1.4 GHz radar penetration and evidence of drainage structures in temperate ice: Black Rapids Glacier, Alaska, U.S.A.

Steven A. Arcone, Norbert E. Yankielun
Cold Regions Research and Engineering Laboratory, U.S. Army Corps of Engineers, 72 Lyme Road, Hanover, New Hampshire 03755-1290, U.S.A.

ABSTRACT. We have tested the ability of a 1.12–1.76 GHz bandwidth airborne Frequency Modulation–Continuous Wave (FM-CW) radar with an effective pulse duration of 3 ns to penetrate temperate ice of the ablation zone of Black Rapids Glacier, central Alaska, U.S.A. We used high-gain horn antennas to suppress clutter, and tested over cold and nearly ideal surface conditions. Englacial horizons dipping to at least 60 m depth were found along three sections of one axial profile. More narrow-band (1.21–1.29 GHz), low-resolution (24 ns pulse duration) profiles from a fourth section detected events at about 100–150 m depth. Comparative profiles recorded with a 100 MHz short-pulse-type radar reproduce the horizons of two of the sections, and verify the penetration in all cases. All horizons are composed of diffractions. We interpret voids from the phase of the 100 MHz diffractions within one of the horizons. The diffraction nature of the horizons, the void interpretation and the proximity to a nearby and up-glacier pothole field lead us to conclude that the horizons within two of the sections are meandering drainage channels. A more complex, branching structure with near-surface horizons profiled within the third section much farther down-glacier may also be a complex drainage system fed by near-surface melting. The FM-CW signal-to-clutter-noise ratios of some of the targets predict that they could be detected at 200 m depth in the 1–2 GHz range. Significant performance improvements at maximum vertical resolution could be achieved with higher-gain antennas.

INTRODUCTION

Understanding of englacial drainage processes in temperate glaciers (Lawson, 1993; Fountain and Walder, 1998) would benefit from a radar technique that could image drainage structures. Water bodies, drainage networks, debris, crevasses and fractures in temperate glaciers scatter energy and limit penetration of radar signals (Smith and Evans, 1972; Davis, 1973; Watts and England, 1976; Bamber, 1988). However, the unwanted backscatter (clutter), manifested as englacial diffractions and out-of-plane hyperbolic reflections seen within depth profiles recorded above 30 MHz (Blindow and Thyssen, 1986; Arcone and others, 1995), may mostly be responses to interesting features related to drainage and whose structure a higher-frequency radar might resolve. Given our present understanding of conduit dimensions (Holmlund, 1988), their resolution would require relatively wide bandwidths centered at frequencies above about 500 MHz (Arcone and others, 1995; Arcone, 1996), for which the in situ wavelengths are about 0.34 m or less.

In this study we describe a continuously profiling Frequency Modulation–Continuous Wave (FM-CW) radar we have developed that radiates a high-resolution pulse whose bandwidth is centered near 1.4 GHz, and discuss airborne tests we have performed on its ability to penetrate temperate ice. We used high-gain antennas whose effective, transmit–receive narrow beam, enhanced by refractive focusing through the air–ice interface, improved radar performance by suppressing subsurface volumetric scattering. We chose an area of apparent ice compression within the ablation zone of the temperate and windy Black Rapids Glacier, central Alaska, U.S.A. We profiled in late winter so that the apparently smooth and marginal snow cover, and the lack of both surface water and apparent crevasses, would minimize near-surface clutter, which could be severe at GHz frequencies. This choice of area might have compromised our chances of detecting drainage channels for test targets, which are believed to develop mainly from crevasses (Fountain and Walder, 1998). Therefore, we first located many profiles near large medial moraines where we hoped to find englacial debris as targets. However, because the FM-CW profiles within the main trunk revealed unexpected horizons that appeared unique and related to drainage, we expanded our investigations with airborne, short-pulse-type radar profiles at 100 MHz to verify their existence, and therefore the FM-CW penetration. We then used the phase of the short-pulse waveforms to help us interpret these horizons because the incoherency of the FM-CW radar precludes waveform resolution. We calculate signal-to-clutter-noise ratios of individual targets within these structures to estimate performance limits, and compare our predictions with the results of deeper profiles obtained with a longer-duration (narrower-bandwidth) pulse centered at 1.25 GHz.

We have chosen to work with FM-CW radar because of its ability to achieve economically a high antenna gain with a very short pulse; its drawbacks will be discussed in sections on data processing and performance and in the Conclusions section. FM-CW radars have been used at bandwidths centered at 1.5–33 GHz to investigate snow (Ellerbruch and Boyne, 1980; Gubler and Hiller, 1984) and firn (Forster and others, 1991) and to continuously profile river and lake ice

https://doi.org/10.3189/172756500781833133 Published online by Cambridge University Press

thickness (Yankielun and others, 1992; Arcone and Yankielun, 1997). The more traditional short-pulse (also referred to as impulse, or transient) radars require low-gain electrically short antennas to form the short-duration pulses. Consequently, their wide beamwidths (Arcone, 1995) reduce their performance because clutter suppression has an inverse dependence on antenna beamwidth (Skolnick, 1980). The penetration depth of short-pulse radars operating above 500 MHz and at necessarily low power has been limited to <30 m on polar glaciers (Glover and Rees, 1992; Arcone, 1996) and on temperate glaciers in late winter (Arcone and others, 1992, 1995). Although high frequencies (840 MHz) and also high-gain antennas (15 dB) have been employed with conventional, high-performance, modulated-carrier radio-echo sounding systems to penetrate 750 m in ice (Narod and others, 1988), polar ice was profiled and much longer pulse durations were radiated. For our purposes vertical resolution would be compromised by this type of system. Synthetic pulse systems have achieved about 100 m penetration in the polar regime of a glacier, but only at a low-resolution bandwidth (950–1000 MHz; Ødegård and others, 1997)

RADAR SYSTEMS

FM-CW principles

The principles of FM-CW radar are well known (Skolnick, 1980, 1990; Stove, 1992). Briefly, a constant-amplitude sinusoidal signal whose frequency increases linearly with time over a duration, t_{swp}, is transmitted (Fig. 1). The received signals, each delayed by the round-trip propagation time, $2t$, are mixed with a sample of the transmitter output. The mixing process produces sum-, Σ, and difference-frequency, Δ, time-domain signals. Low-pass filtering retains only Δ, whose Fourier transform is $\mathscr{D}$. The frequency, f, of each component of $\mathscr{D}$ is proportional to the range, R, of a specific target. The spectrum of $\mathscr{D}$ is usually within audio-range bandwidths. The relationship between the bandwidth, B, of the transmitted signal and f is

$$B/t_{swp} = f/2t \quad (1)$$

and is illustrated for a single target in Figure 2. For a homogeneous medium, R and t are related by

$$t = Rn/c\,, \quad (2)$$

where c is the velocity of light in a vacuum (3×10^8 ms^{-1}) and n is the index of refraction of the medium. For low-loss media such as ice ($n = 1.78$), n is the square root of the relative dielectric permittivity. Combining Equations (1) and (2) gives

$$R = ft_{swp}c/2Bn\,, \quad (3)$$

which shows that higher-frequency spectral components represent greater range. With the use of Equation (2), discrete spectra can be interpreted as a train of time-domain pulses returning from discrete targets.

FM-CW system fabrication

The radar system is diagrammed in Figure 1. Previous configurations at other bandwidths have been reported elsewhere (Yankielun and others, 1992; Arcone and Yankielun, 1997). A frequency-sweep signal oscillator provided 32 mW of continuous power from 1.12 to 1.76 GHz directly to the transmitter antenna using standard coaxial cable (Fig. 3). We used a portable

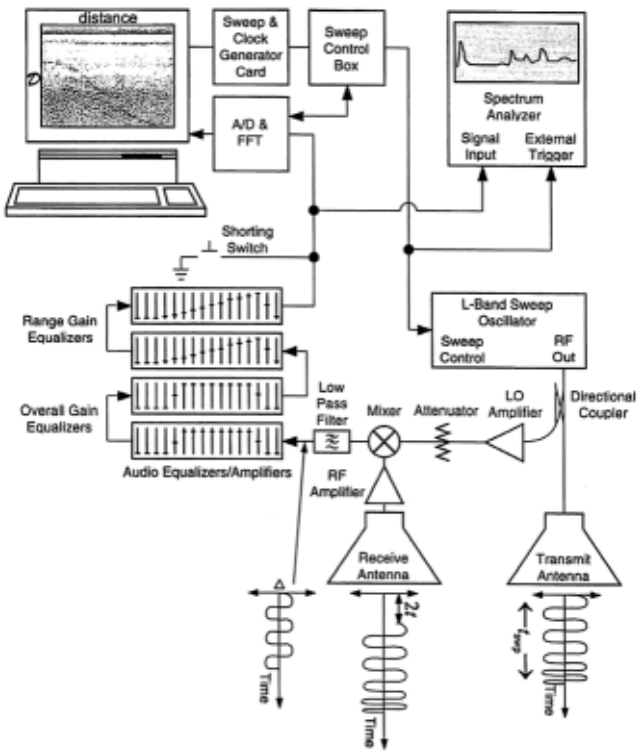

Fig. 1. Signal generation and transformations in FM-CW radar and a diagram of our L-band system. Consecutive traces of the power spectrum $\mathscr{D}$ are displayed to produce a reflection profile.

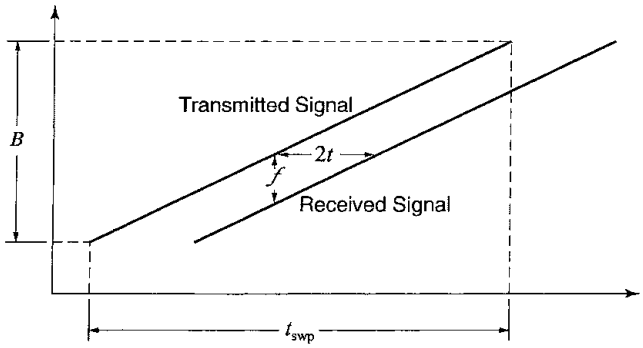

Fig. 2. The time and frequency relationship between the signal spectrum transmitted by an FM-CW radar and that received from a single target. The difference between the two spectra is constant in time for a simple reflecting surface.

Fig. 3. The FM-CW radar system mounted to a Bell Jet Ranger 206B helicopter. Receiver components are mounted in a small box between the antennas. A coaxial cable from the helicopter window feeds power to the transmitter.

https://doi.org/10.3189/172756500781833133 Published online by Cambridge University Press

personal computer to set t_{swp} and B, and drove the oscillator between the band limits with a 0–10 V ramp, generated by timing signals synchronized with the digitization of the received signal (discussed later). We kept the oscillator in the helicopter cabin. We used standard-gain L-band horns for the transmitter and receiver antennas and separated the edge of their apertures by approximately 0.05 m.

The received radio-frequency signal was amplified by 20 dB and directed to one port of the mixer. A directional coupler provided the low-level reference signal from the sweeper to the other input port. We used a preamplifier and a fixed attenuator to adjust the reference signal level to meet mixer specifications. A low-pass filter passed only Δ, whose frequency components are typically in the 0–20 kHz range. We housed the receiver components in a metal enclosure mounted between the transmitter and receiver antennas (Fig. 3).

We fed the Δ signal to four stages of graphic audio equalizers located in the helicopter cabin. The first two stages supplied level gain across the full Δ bandwidth, a low-pass filter to anti-alias the signal prior to the acquisition and digitization process, and a high-pass filter to attenuate the dominant direct coupling signal. The −3 dB frequency for the low-pass filter equaled half the digital sampling frequency, as dictated by the Nyquist criterion (Oppenheim and Schafer, 1975). We set the −3 dB high-pass frequency to approximately 500 Hz to prevent saturation of the digitizer by the direct coupling. This filter thus allowed greater dynamic range and amplification of the higher-frequency components (Fig. 4). We configured the next two stages to provide an optional increasing gain with increasing frequency (equivalent to the time-variable gain of time-domain, pulsed systems; also referred to as "range gain"). This gain was not used during recording because it did not improve the quality of the recorded data. However, range gain was applied during post-processing.

We directed the amplified and filtered Δ signal to a 16-bit digitizer at either 12 or 24 traces per second and stored each trace as a vector of N (1024) sample points. N was fixed by the sample rate, f_s, which was determined by the clock circuit of the digitizer. We used $t_{swp} = 33$ and 66 ms at 24 and 12 traces per second, respectively. These values accommodated N and f_s according to the relationship

$$t_{swp} = N/f_s\,. \tag{4}$$

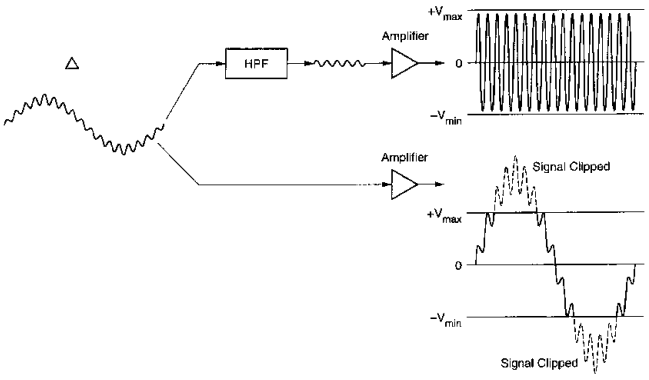

Fig. 4. A representation of the range problem caused by direct coupling. The received signal, Δ, at left contains high-frequency, long-range signals superimposed on the low-frequency direct coupling. The long-range signals will not be accurately digitized (right, bottom) until the low-frequency signal is removed by the high-pass filter, HPF (right, top).

Our memory storage had limited capacity, so the file size had to be estimated and preset before a profile was recorded. Therefore, we used 12 traces per second only for a very long profile we recorded at a bandwidth of 1.21–1.29 GHz to search for deep returns, because it compromised data quality.

Combining Equations (3) and (4) gives

$$R = Nfc/(2Bf_s n)\,. \tag{5}$$

Equation (5) shows that R can be increased either by reducing B or by increasing N. Reducing B effectively produces a longer time-domain pulse and a corresponding loss in vertical resolution. Alternatively, for a given t_{swp}, N can be increased by increasing the sampling rate, f_s, which requires a higher-order fast Fourier transform (FFT) and longer computation time. The bandwidth of 1.12–1.76 GHz translates to a range of 67 m in ice with the digitization and FFT parameters used. The bandwidth 1.21–1.29 GHz theoretically gives 539 m.

During profiling, we monitored the sample sequential time series and FFT traces in real time with an HP 3560 Dynamic Spectrum Analyzer (Fig. 1). This allowed us to adjust the signal gain manually to prevent saturation of the digitizer. Simultaneously, fiduciary marks corresponding with global positioning system (GPS) positions recorded on the aircraft GPS navigation system were manually added to the radar record.

FM-CW antenna gain

The single antenna −3 dB beamwidth in both principal radiation planes is approximately 26°, and the antenna gain is about 18 dB at the center of the frequency sweep. Refraction across the air–ice interface decreases this beamwidth to about 14.5°. This concentration of energy, when translated back to the aperture plane of the receiver antenna, enhances the gain and can be expressed as an energy focus factor Φ (Bogorodsky and others, 1985), which approaches 3.3 for our beamwidth as the depth becomes much larger than the aircraft altitude. For our nominal aircraft height of 6 m, this factor was about 2.6–2.8 for the target depths (30–50 m) of analytical interest, and increased the antenna gain in the forward direction to about 23 dB. The electric-field plane of the antennas was parallel to the helicopter skids (Fig. 3) and therefore to the forward motion of the helicopter and the direction of profiling.

FM-CW post-processing

We first passed the Δ signals through a Hanning window to reduce spurious spectral side lobes generated by the FFT. We display the amplitude of the real part of the FFT in a spectral format (Fig. 5) calibrated for range using Equation (3). Although coherent FM-CW radar is feasible by processing the entire complex FFT, the complex FFT spectrum is range-dependent. Therefore, the phase relationships between the pulse spectral components, and consequently the pulse shape, would not be maintained as the target depth changes. The FFT traces were then compiled as a continuous reflection profile of distance vs range, or its equivalent time delay. When calibrated in the time domain, a spectral peak formed from the 1.12–1.76 GHz bandwidth has an effective −3 dB time-domain pulse width of ~3 ns. The width increases in inverse proportion to the bandwidth; at 1.21–1.29 GHz it is about 24 ns.

We used a commercial software package to further process the FFT profile traces in the equivalent time-domain

https://doi.org/10.3189/172756500781833133 Published online by Cambridge University Press

calibration. We applied high-pass frequency filtering to alleviate an unwanted but small amplification that increased linearly with time delay and produced noise streaks in the record. The filter also transformed the positive pulses into Ricker-type $1\frac{1}{2}$-cycle wavelets (Sheriff, 1980). The phase polarity sequence of these wavelets has no relation to any target or interface reflectivity (Arcone and others, 1995) because it is an artifact of the processing (Fig. 5). We then normalized the position of the glacier surface reflections within the profiles, which varied because of changes in aircraft altitude. Finally, we made an approximate glacier surface-elevation correction based on published values of the surface slope in our study area.

FM-CW dynamic range and performance

Despite the high antenna gain, the system is a low-performance radar. At 16-bit quantization the theoretical dynamic range of any trace is 96 dB. The sample quantization noise reduced this value to a measured 87 dB. Noise caused by the electronic components, and the very low level of transmitter power required to limit the levels of direct coupling between antennas and the direct feed to the mixer, reduced the range further, to about 70 dB (Fig. 6). This value is therefore also the performance figure (Skolnick, 1990) because it is the difference between the maximum detectable field strength before saturation and the system noise floor. The value is low compared with more standard and more expensive time-domain pulsed systems (Gogineni and others, 1998). Table 1 summarizes the system parameters.

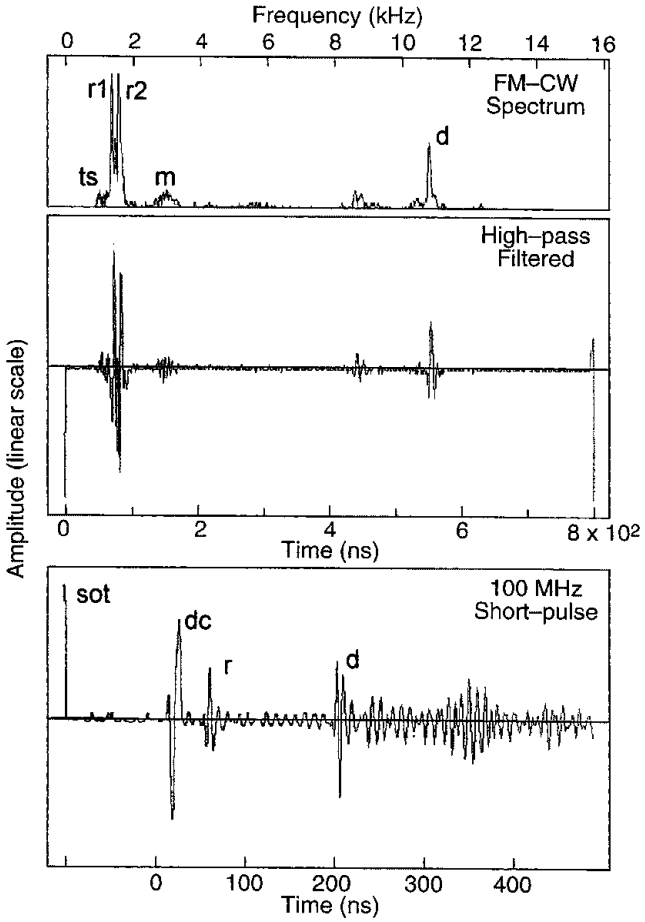

Fig. 5. Received and filtered waveforms of the FM-CW and 100 MHz short-pulse radar systems. A spectrum of the FM-CW difference frequency time signal (top) and its high-pass filtered version (middle) are interpreted as a trace of pulses delayed in time. Events in the top trace are: time side lobe (ts), snow-surface reflection (r1), ice-surface reflection (r2), multiple reflection between surface and helicopter (m) and subsurface diffraction (d). The direct coupling is suppressed by filtering. The time side lobe is an artifact of the Fourier transformation, and the spikes at the start and end of the middle trace are artifacts of the post-processing. Events in the 100 MHz trace (bottom) are: start of trace signal from the transmitter (sot), direct coupling between the transmitter and receiver antennas (dc), surface reflection (r) and subsurface diffraction (d). Note the change in phase between events r and d.

100 MHz short-pulse system

We recorded profiles with a 16-bit short-pulse radar system (GSSI, model 10a+) using 100 MHz (model 3107 at 42 W peak transmitter power) antennas along the same transects for comparative purposes. Despite the lower directivity of the 100 MHz antennas, the system provided comparable penetration because of the longer wavelength and higher transmitter power. We also recorded a 500 MHz profile, but the

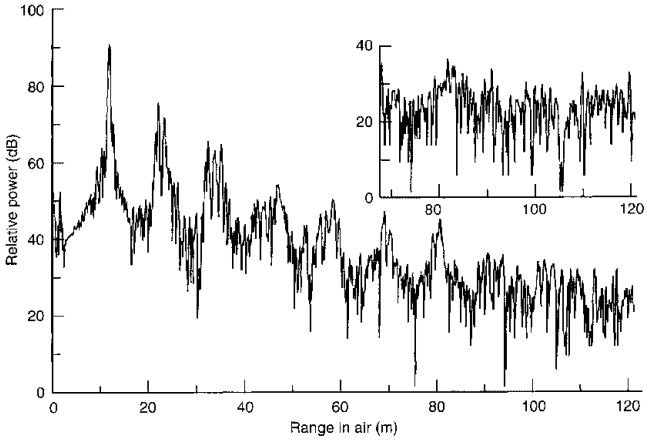

Fig. 6. Calibration traces obtained for estimating FM-CW system performance and dynamic range. The full trace is a recording of a primary reflection from a water surface at a range of 11.5 m, and subsequent multiple reflections between the water surface and the bridge platform. The peak signal level, at about 90 dB, is just below saturation. At far range the noise level is about 70 dB below the peak level. The inset shows a portion of a sky calibration (antennas pointed toward the sky) obtained at the same time. The noise is internal and not from clutter. No range gain was used in the recordings.

Table 1. FM-CW radar system parameters

Input power, P_t	32 mWHz^{-1}
Transmit bandwith, B	1.12–1.76 GHz (hi-res.)
	1.21–1.29 GHz (low-res.)
Range (max.) in ice, D	67 m (hi-res.)
	539 m (low-res.)
Antenna gain, G	18 dB
II* bandwith	0.5–20 kHz
Dynamic range (est.)	70 dB
Data acquis. rate	12, 24 traces per second
Sweep time, t_{swp}	0.0655, 0.0328 s
Sample rate, f_s	15 675, 31 250 Hz
Trace density, N	1024
Trace sample quant.	16-bit

*Intermediate frequency.

https://doi.org/10.3189/172756500781833133 Published online by Cambridge University Press

maximum time range allowed by the system parameters (400 ns) is too short to permit a meaningful comparison of performance. The resistively loaded dipole antennas were mounted beneath the cabin and polarized perpendicular to the aircraft axis (and flight direction) in order to decrease the intensity of aircraft reflections. The effective two-way, radar −3 dB beamwidth in air of about 70° (Arcone and Delaney, 1987) narrows to about 38° after refraction within ice and provides a transmit–receive antenna gain of about 15 dB. We recorded 24 traces per second (same as the FM-CW), and range gain was always used. We processed the profiles with horizontal, spatial filtering to reduce severe interference from the helicopter fuselage, and with a Hilbert magnitude transform (Sheriff, 1980; Long and others, 1995) to capture the envelope of the events because their phase and amplitude variability make them difficult to view at the long time range used. We estimate the performance figure of this system to be about 100 dB.

A 100 MHz profile trace is shown in Figure 5. This trace was selected because the surface reflection shows the form of the transmitted pulse; most other surface waveforms show interference between snow and ice surface reflections. The phase polarity of the transmitted pulse is reversed in the reflection from the surface. A reflection or diffraction from an interface between air below and snow or ice above will not invoke this phase polarity change. We use the phase polarity sequence of the amplitudes of the stronger half-cycles (− + −) to reference the phase of subsurface diffractions discussed later. There is no phase polarity change upon transmission through an interface. Interpretation of dielectric contrasts from phase polarity changes is discussed more extensively by Arcone and others (1995) and Arcone (1996).

TEST SITE

Black Rapids Glacier (Fig. 7, top) is located in central Alaska within the Alaska Range. It is approximately 41 km long, 2–3 km wide and is fed by several tributary glaciers, mainly from the south, which have pushed large medial moraines into its main trunk. It had a major surge in 1937 (Hance, 1937). At present it is retreating. The equilibrium line is placed by Heinrichs and others (1996) at about 146°30′ W, which is at the west end of our study area and is at approximately 1680 m (5500 ft) a.s.l. The accumulation zone along the main trunk contains an extensive field of potholes (Sturm, 1987; Sturm and Cosgrove, 1990), the diameters of which may be as large as 50 m. Several of these potholes are near two sections we profiled (Fig. 7, bottom), and potholes in this vicinity were observed by Sturm and Cosgrove (1990) to be interconnected through subsurface channels that had to be several hundred meters long. Temperature profiles reported by Harrison and others (1975), one of which was within our study area, show that the ice in late winter is within one degree of 0°C by 10 m depth, and should reach 0°C by 15 m depth. The trend of these temperature–depth profiles led Harrison and others to favor a temperate classification for Black Rapids Glacier.

The profiled sections (S1–S4) to be discussed are indicated in Figure 7. The 1949 and 1972 snowlines (Sturm, 1987) pass through S3, while the equilibrium line is west of S3. Therefore, S1 and S2 are entirely in, and S3 is at least partly within, the ablation zone. S1–S3 are part of a longer axial transect that began at the east end of S1, ran west approximately parallel to the center-line coordinate system within the 14–22 km distances of Heinrichs and others (1996), and are the only sections along this line in which horizons were recorded. By "horizons" we mean any combination of reflection segments or diffractions that provide some continuity in a radar profile. Several across-glacier profiles (Fig. 7), three of which intersected the axial sections, do not show any horizons. The central flowline annual speed is about 40–70 m a^{-1}, and the ice depth is about 600–700 m in the vicinity of S1–S3. Both S2 and S3 are within 1–1.5 km downglacier of the above-mentioned pothole field. At S4 (38 km distance of Heinrichs and others, 1996), the glacier speed is about 10 m a^{-1}, and the depth is about 240–280 m. We used a surface slope of 0.025 in the area of S1–S3 (Raymond and others, 1995) to give an approximate elevation correction to our profile interpretations.

All sections appear to be in areas of compressional flow. S1 lies in an area dammed by steady flow from the north-flowing Loket tributary entering at about 146°20′ W (Heinrichs and others, 1996). S4 is in a section of uncrevassed and mostly bare ice that is bounded by heavy surface debris. There is no indication of crevassing, such as strong near-surface diffractions or dipping snow-bridge strata (Delaney and Arcone, 1995), in any of our profiles, but Sturm and Cosgrove (1990) observed numerous crevasses about 1 km west of S3. An enlargement of the high-altitude photography of Figure 7 appears to show sutured crevasses, and possibly widely spaced active or fossil moulins in the area of S1–S2. No crevasses along or across S2 and S3 are apparent in the more detailed photography of Figure 7 (bottom).

The wind-blown snow cover appeared smooth over all these sections during profiling, but a quantitative assessment of smoothness is given later because it is pertinent to the short FM-CW wavelengths used. The FM-CW profiles generally indicate a 1 m snow layer along sections S1–S3 and slightly more than 2 m at the highest elevations of the main trunk. This was a winter of little snow accumulation in interior Alaska, and there were many areas without snow cover, especially along S4, in the lower reaches of the main trunk, but this may be common due to the high winds. Although the snow surface appeared smooth over all sections, the late-summer pothole photography of Figure 7 shows that the ice-surface conditions may have been much different.

RESULTS AND DISCUSSION

The FM-CW profiles along S1–S3 (Fig. 7) were recorded in late March 1996 at a maximum vertical resolution (1.12–1.76 GHz; 3 ns effective pulse duration), which fixed our maximum recorded penetration in ice at about 60 m after loss of time caused by the pulse delay in air. The FM-CW profile over S4 was recorded at greatly decreased resolution (1.12–1.29 GHz; 24 ns pulse duration), which allows far greater potential penetration (>500 m). The profiles over S1–S3 were recorded at 24 traces per second while moving up-glacier into 3a headwind. The profile over S4 was recorded at 12 traces per second moving downwind. Helicopter altitude above the glacier surface was 6–9 m, and airspeed was 6–8 m s^{-1} when profiling up-glacier. No roll, pitch or yaw of any significance occurred during the flights, so the antenna boresights (axes) were always near vertical. We recorded the profiles with each system on separate runs that ran between preset waypoints on the aircraft GPS navigation system. The estimated accuracy of this system (30 m) and variations in flight speed make it unlikely that the compared profiles followed exactly the

https://doi.org/10.3189/172756500781833133 Published online by Cambridge University Press

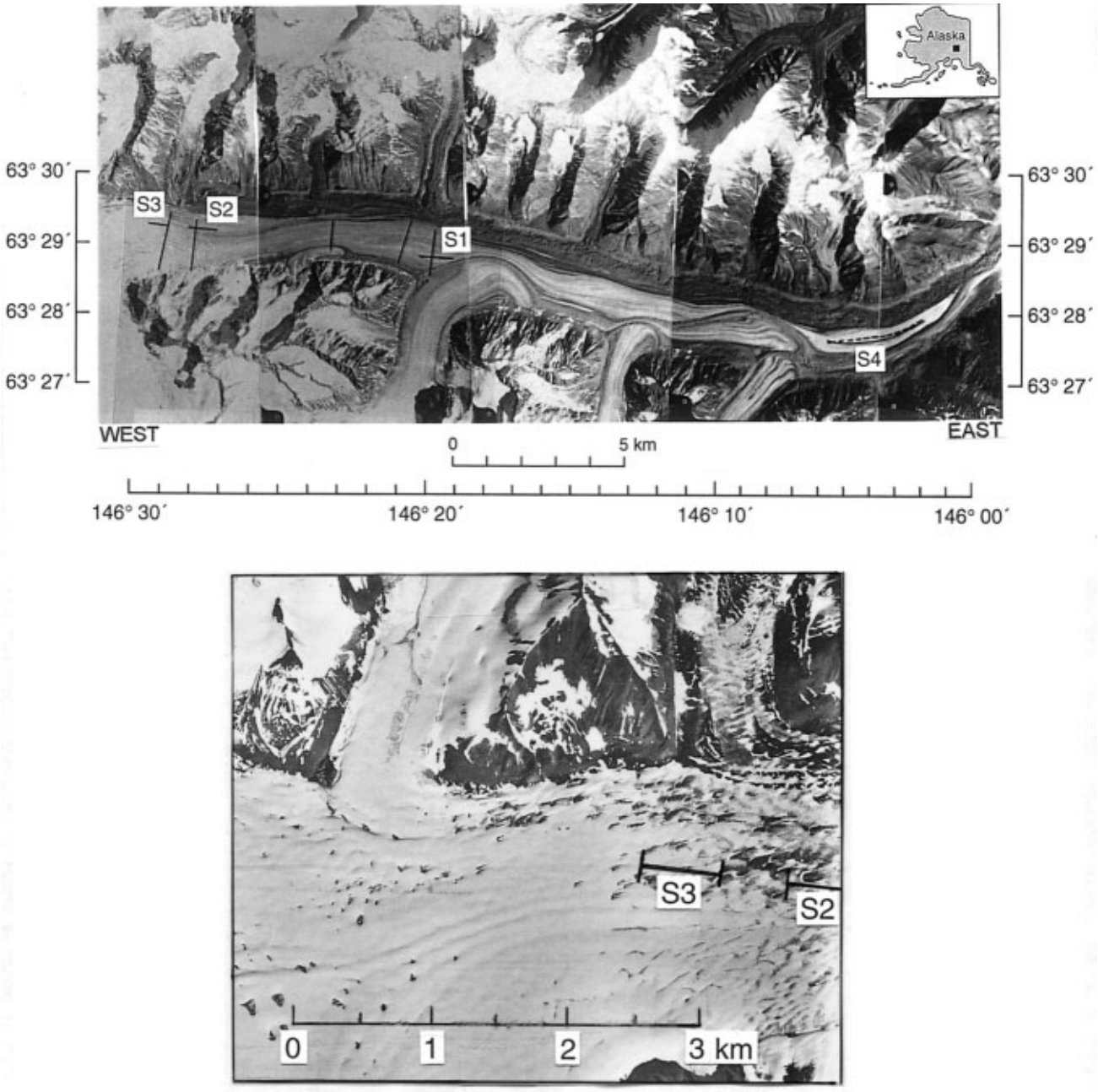

Fig. 7. Top: Locations of the axial and across-glacier transects profiled along Black Rapids Glacier. The axial solid lines denote the FM-CW and 100 MHz transects, S1–S3; the dashed line denotes that of the 100 MHz radar along S4. The glacier flows eastward. The glacier photographs (line 85, frames 8502-07, NASA High Altitude Aerial Photography Program, Alaska) were obtained on 5 August 1980. The coordinates are translated from the U.S. Geological Survey Mount Hayes (B-5) 1:63 360 quadrangle topographic map (limited revisions 1978). The longitudinal scale becomes slightly compressed towards the east to accomodate photographic distortion. Bottom: Detail of the pothole field near S3 (photo courtesy of M. Sturm).

same line or covered exactly the same distance. However, the presence of survey flags (not ours) along sections S1–S3 allowed most of the FM-CW profile to be repeated accurately with the 100 MHz radar.

Below, we display the FM-CW profiles in an amplitude format whereby positive amplitudes are white and negative are dark. We also display the 100 MHz profiles in an amplitude format, but because of the Hilbert transformation process all signals are displayed in light (positive) tones. We refer extensively to the diffractions apparent in the FM-CW profiles. These are isolated, or nearly isolated, events with a near-hyperbolic shape. The slopes of their asymptotes, where measurable, indicate responses to localized targets, rather than to linear features that obliquely crossed the transects (Clarke and Bentley, 1994), because they correspond with the refractive index for ice.

Section S1

We compare the FM-CW and 100 MHz short-pulse radar profiles and present a line interpretation in Figure 8. The 100 MHz profile has greater depth range because of the longer time range used. Both profiles show nearly the same structure, which validates the FM-CW results. However, the FM-CW profile more clearly shows the diffraction nature of the horizons, even though the narrow beamwidth abbreviates their asymptotes. The diffraction events do not appear to be in multiples, although a few occur in vertical succession. The heavy arrows indicate faint, dipping horizons of diffractions that start near the surface and extend to about 8–10 m depth. The horizons we have labeled a, b and c appear to be most extensive. The centralized horizon, a, extends across most of the profile. It peaks in height at 11 m

https://doi.org/10.3189/172756500781833133 Published online by Cambridge University Press

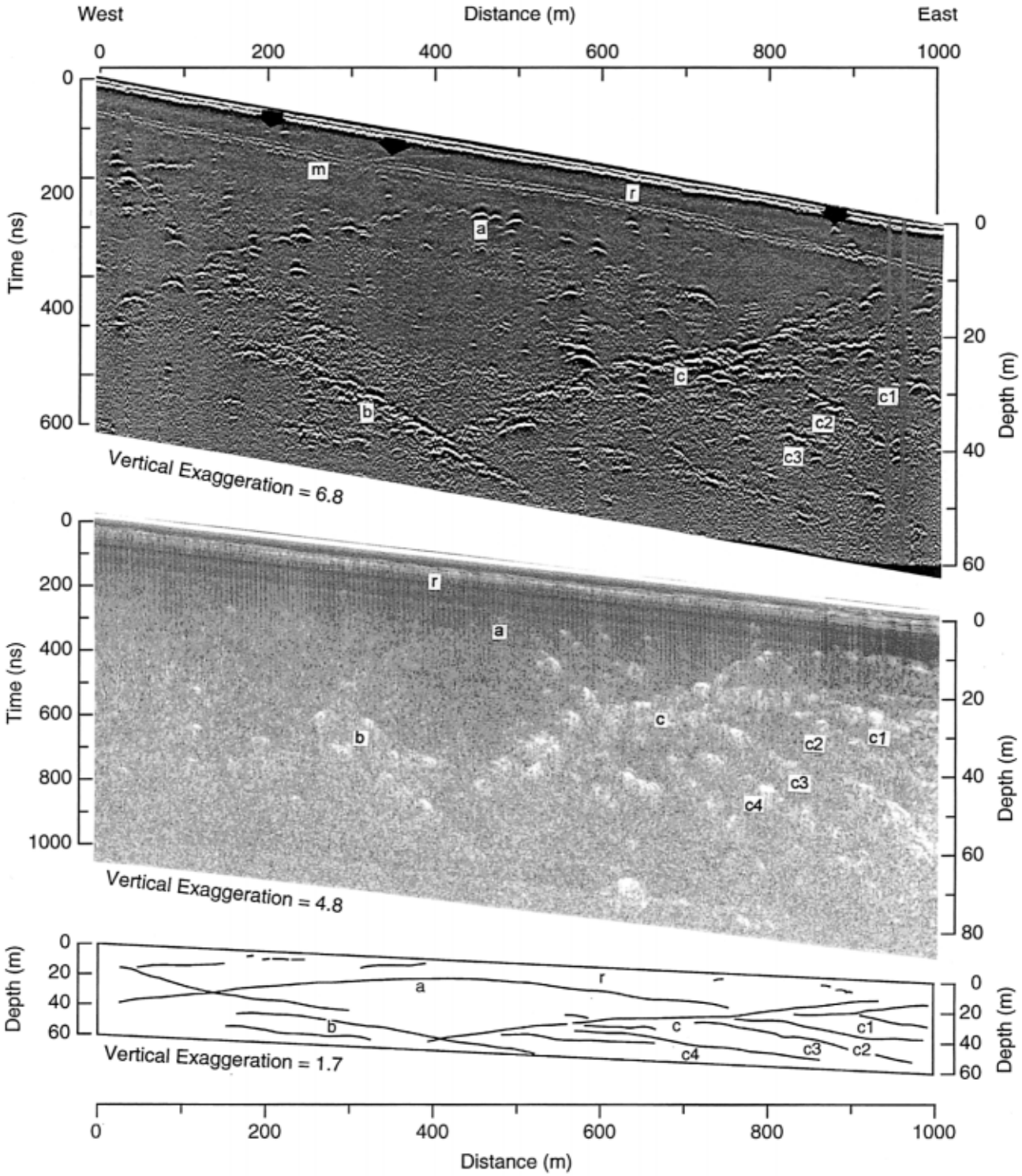

Fig. 8. FM-CW (top) and 100 MHz short-pulse profiles (middle) of S1, and line interpretation based on the FM-CW profile. Labels are beneath their respective horizons, which are: surface reflection (r), multiple reflection between the surface and the aircraft (m), extended horizons (a, b, c), and branching horizons (c1–c4). Arrows in the FM-CW profile indicate faint horizons near the surface. The surface reflection and its multiple (not visible) in the 100 MHz profile are attenuated by the horizontal noise filtering.

depth at about the 450 m distance, and then appears to connect at about 25–30 m depth with other prominent horizons at 120 (horizon b) and 800 m distances (horizon c), of which b dips down-glacier and c dips up-glacier. Horizon b extends to the bottom of the record, which shows that the GHz signals penetrated at least 60 m. This depth would include about 45 m within the temperate ice beneath the winter regime. In the right half of the profile, horizon c appears to connect with at least four branches (c1–c4) that dip to the east (down-glacier). Although some of these branches steepen with depth, the decreased vertical exaggeration in the line-drawing interpretation shows that all horizons have a shallow dip angle. For example, horizon b dips about 3.8° relative to the surface and 5.2° relative to horizontal.

Section S2

The FM-CW profile of S2 (Fig. 9) has only one strong horizon, a, and a faint parallel horizon, b, about 45 ns later. Horizon b is probably a multiple reflection of horizon a that occurred between the helicopter and the glacier surface because the delay of horizon b relative to a is consistent and similar to the delay of horizon m. The diffractions along

https://doi.org/10.3189/172756500781833133 Published online by Cambridge University Press

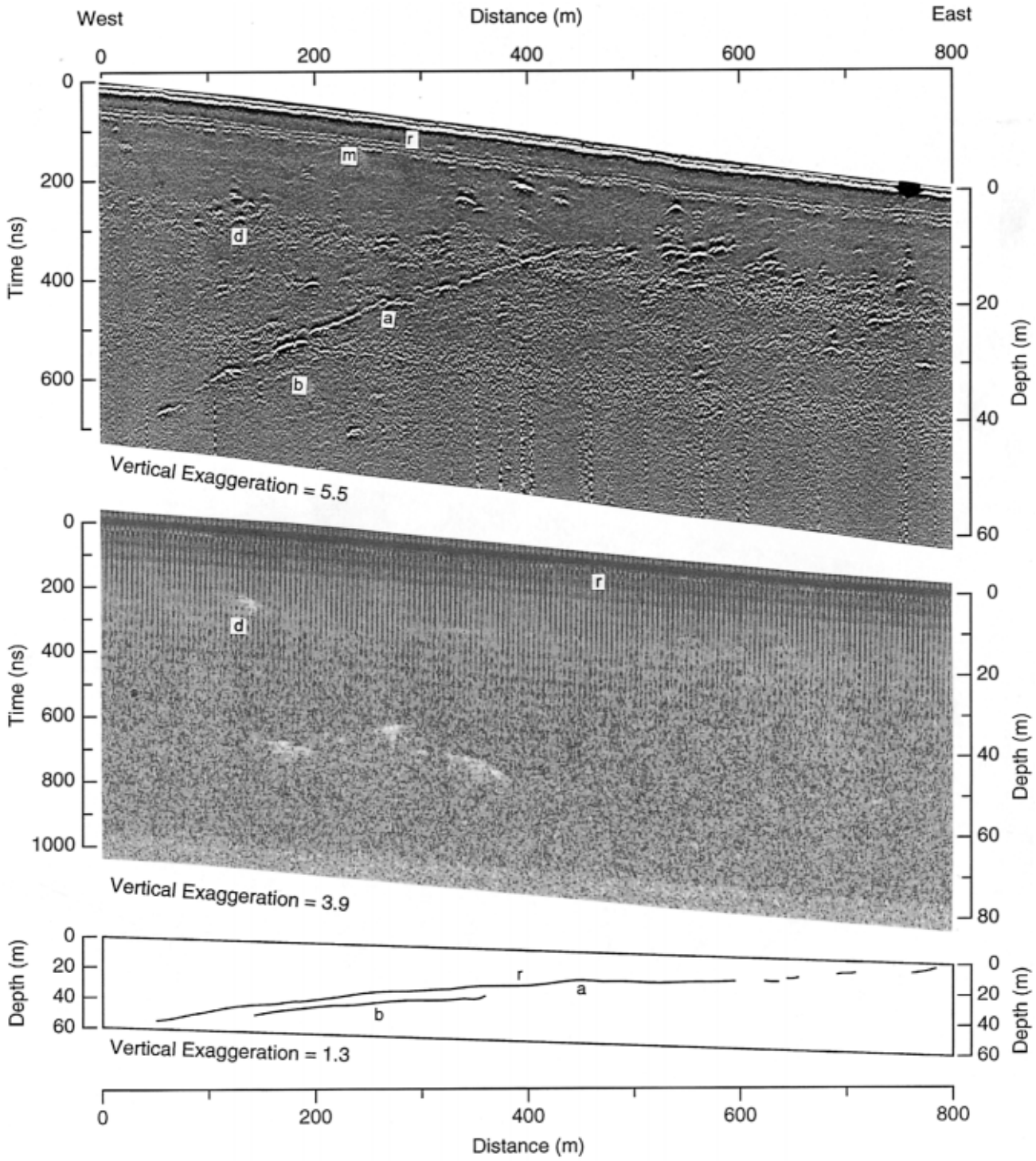

Fig. 9. FM-CW (top) and 100 MHz short-pulse profiles (middle) of S2, and line interpretation based on the FM-CW profile. Horizon notation is the same as in Figure 8, with the addition of d, a cluster of diffractions.

horizon a are closely spaced and so form an almost continuous reflection horizon that is nearly straight between 100 and 400 m. The slope of this section is 4.6° relative to the surface and about 3.2° relative to horizontal. As with horizon c of S1, this horizon dips in the up-glacier direction, and it can be followed to the surface (arrow). We also identify a small cluster of diffractions (d) because they correspond in depth (15 m) and distance (120 m) with events seen at 100 MHz.

In contrast with the similarity between the profiles of S1, we cannot identify any horizon in the 100 MHz profile that corresponds with a in the 1.4 GHz profile. However, it is clear that this section provided interesting targets at 100 MHz as well. All the major 100 MHz events occur at about 8–20 m greater depth than the events at corresponding distances at 1.4 GHz. We speculate, therefore, that either horizon a contained narrow targets (long dimension parallel to glacier axis) to which the electric field direction (across glacier) of the 100 MHz signal was insensitive, or the two flight paths over this section deviated slightly. The co-registration of the d events and the similarity of the profiles for nearby S3 suggest that the two up-glacier flight paths were mostly off track here, and then back on track by 130 m distance along S2.

Section S3

The FM-CW profile of S3 (Fig. 10) shows two prominent horizons, a and b; a appears to connect with b. These horizons are barely visible in the 100 MHz profile because of both weaker responses to these targets and the high clutter level. At about 70–90 ns beneath b is a fainter, parallel horizon, c. Careful

https://doi.org/10.3189/172756500781833133 Published online by Cambridge University Press

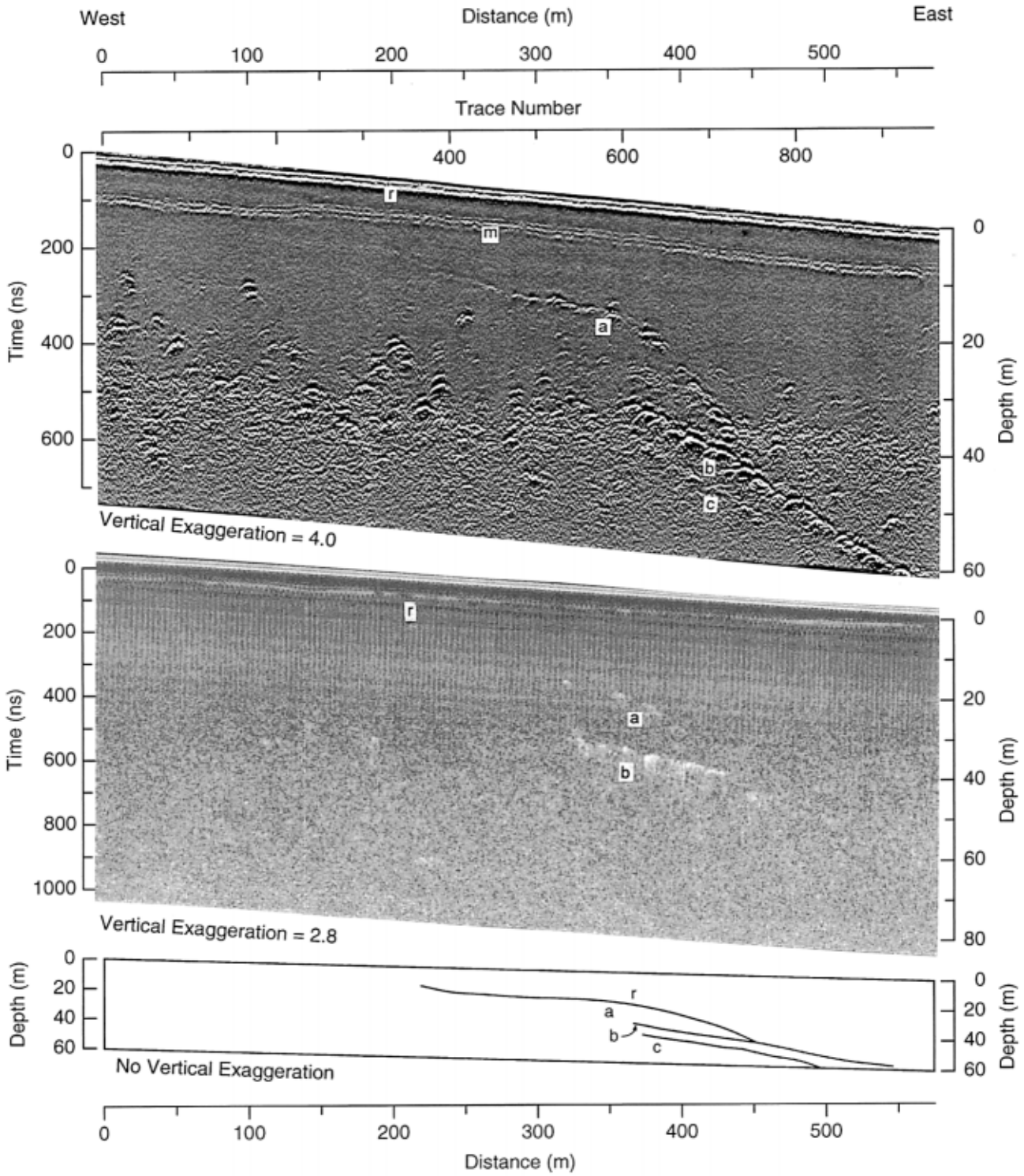

Fig. 10. FM-CW (top) and 100 MHz short-pulse profiles (middle) of S3, and line interpretation based on the FM-CW profile. Horizon notation is the same as in Figure 8.

observation shows that some of the diffraction apices of c align vertically with those in b, and the delay of c relative to b is very similar to that of m relative to r. Therefore, as with section S2, horizon c is probably a multiple reflection of horizon b between the helicopter and the glacier surface. FM-CW horizon b contains the strongest diffractions, with visible asymptotes at 600–800 m distance. The slope of horizon b is about 8.3° relative to the surface and about 9.7° relative to horizontal. The steepest part of horizon a is about 16.5° relative to horizontal. Between 370 and 550 m, about 18 separate diffractions appear along horizon b. The strongest of these occur below 40 m depth, and the deepest at about 60 m depth at lower right.

The traces in which the strongest events of horizon b occur are compared in amplitude format with the 100 MHz traces from nearly the same positions in Figure 11. The traces are compensated for signal strength lost to spherical beam spreading. The ratio of power (computed from the area under the trace of the reflected energy) between the FM-CW target and the surface events (snow and ice reflections), β_{rg} ("rg" stands for range gain added), varies from 0.17 for trace 754, to 0.50 for trace 701. These values are used later to estimate target size. The signal-to-noise ratios in the range vicinity of these events are about 30–45 dB (Fig. 12); the ratios within the 100 MHz traces are considerably less (8–20 dB). We interpret this noise to represent clutter, which is the white speckle visible in the profile display of Figure 10. These levels imply that approximately 200 m of FM-CW penetration are possible in

https://doi.org/10.3189/172756500781833133 Published online by Cambridge University Press

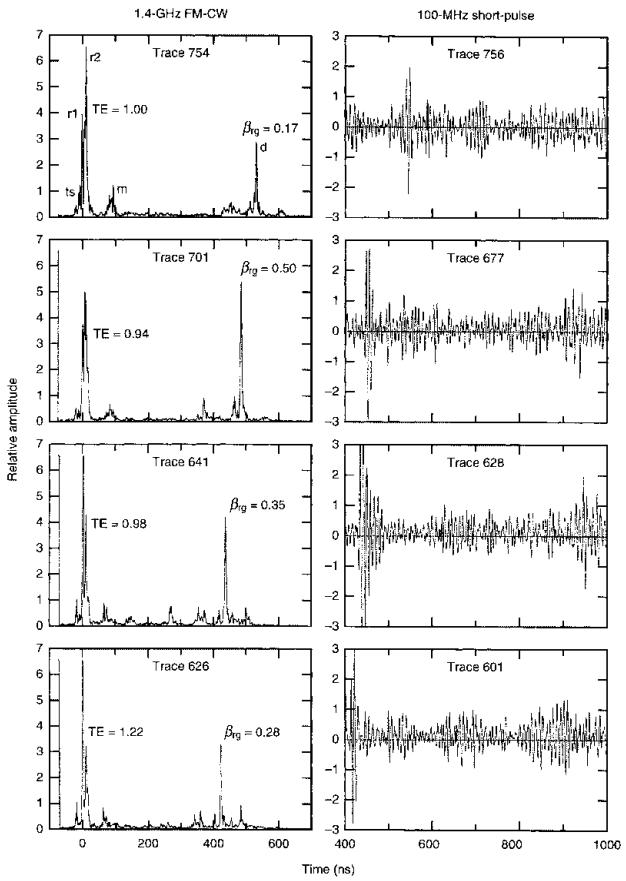

Fig. 11. Amplitude traces from the FM-CW (left column) and 100 MHz (right column) profiles of S3. The FM-CW time reference is for the start of the surface reflection. The 100 MHz traces are of the last 600 ns of the record. The FM-CW frequencies of the surface signals are above the 500 Hz attenuation cut-off. Event notation for trace 754 is the same as in Figure 5 and applies to all other FM-CW traces. TE is the total energy of the surface events, relative to those of trace 754.

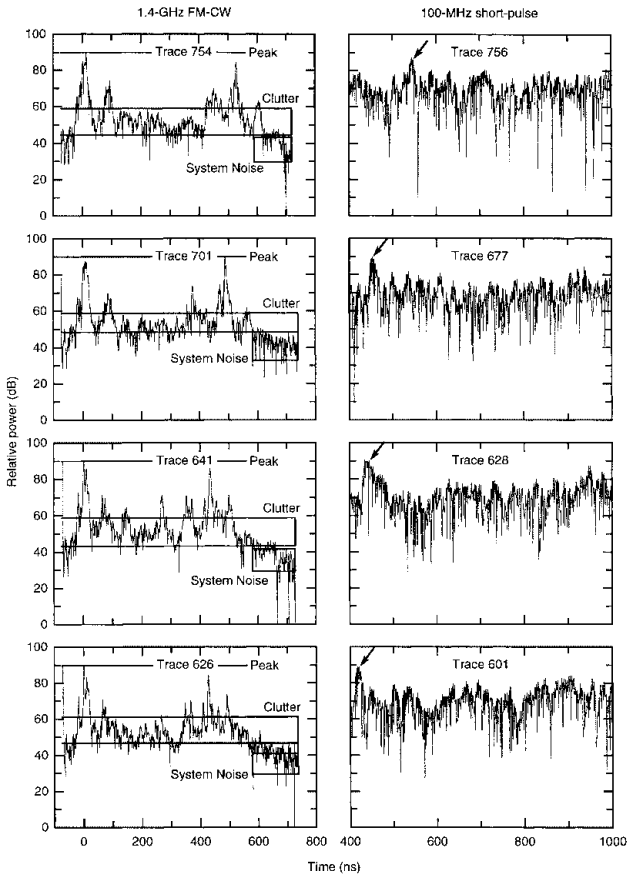

Fig. 12. Power levels for the FM-CW (left side) and 100 MHz (right side) traces of Figure 11. Boxed areas represent the estimated ranges of the clutter and system noise levels. Arrows indicate the horizon b diffraction events.

this ice with our antenna gain before $1/R^4$ attenuation for a small target would bring the signal to within about 3 dB of the maximum clutter level (e.g. trace 701 (Fig. 11), event d at 41 m depth (490 ns) and about 30 dB above clutter). The lowest FM-CW noise levels occur near the ends of the traces and are about 42–60 dB below the peak signal levels. These lowest levels most likely represent the system noise (Fig. 6).

Although a calculation of target-to-signal strength could not be made for the 100 MHz traces because the amplitudes of many surface wavelets were affected by the spatial filtering mentioned above, the phases of the target responses are of analytic advantage. The first major half-cycle of each of the englacial 100 MHz responses is positive, which is opposite that of a primary surface reflection (Fig. 5, bottom). This means that the target is of lower permittivity than the ice, and the only choice is air.

Despite the smooth appearance of the snow surface, it is not obvious that the snow and ice surfaces were smooth relative to the FM-CW wavelengths. This is an important point for profiling at this bandwidth because surfaces with an rms roughness of at least a quarter-wavelength (Rayleigh criterion: Beckmann and Spizzichino, 1963), or even less (Calvo-Perez and others, 1999), can cause strong signal loss by surface scattering. We justify our observation of locally smooth conditions with an analysis of the snow and ice surface reflections (r_1 and r_2, respectively) in the FM-CW traces of Figure 11. Their separation of approximately 10 ns is equivalent to about 1.2 m thickness for a snow layer for which $n = 1.3$ at an assumed density of 0.4 kg m^{-3} (Cumming, 1952). This is a dense value, as would be caused by wind hardening. The relative reflection amplitudes vary widely, from a weaker snow reflection ($r_1/r_2 = 0.6$ for trace 754) to a stronger one ($r_1/r_2 = 2.0$ for trace 626). A wide variation is also predicted by the Fresnel coefficients of plane-wave layer theory (Wait, 1970) for small changes in snow density. For example, an increase in snow density from 0.4 to 0.5 ($n = 1.4$) increases the ratio of the interface reflected amplitudes, $\rho_{as}/(\tau_{as}\tau_{as}\rho_{si})$ from 0.85 to 1.44, where ρ_{as} and ρ_{si} are the amplitude reflection coefficients for the air/snow and snow/ice interfaces, respectively. The quantity $\tau_{as}\tau_{sa}$ accounts for the two-way transmission through the snow surface, where τ is an amplitude transmission coefficient. Regardless of snow depth, the small range of the total energy of the surface events, derived from the total area under the power traces of the waveforms and noted in Figure 11, is also consistent with plane-wave theory for minor changes in snow density. Therefore, the predictability of these data calculations from plane-wave theory implies that the rms roughness of the air/snow and snow/ice interfaces over the antenna surface beamwidth (2–3 m) were much less than an in situ snow wavelength (0.15 m), as it appeared, and therefore did not significantly degrade transmission through the surface layer.

Section S4

We compare FM-CW and 100 MHz profiles for this section in Figure 13 to show some deeper targets detected with the FM-

https://doi.org/10.3189/172756500781833133 Published online by Cambridge University Press

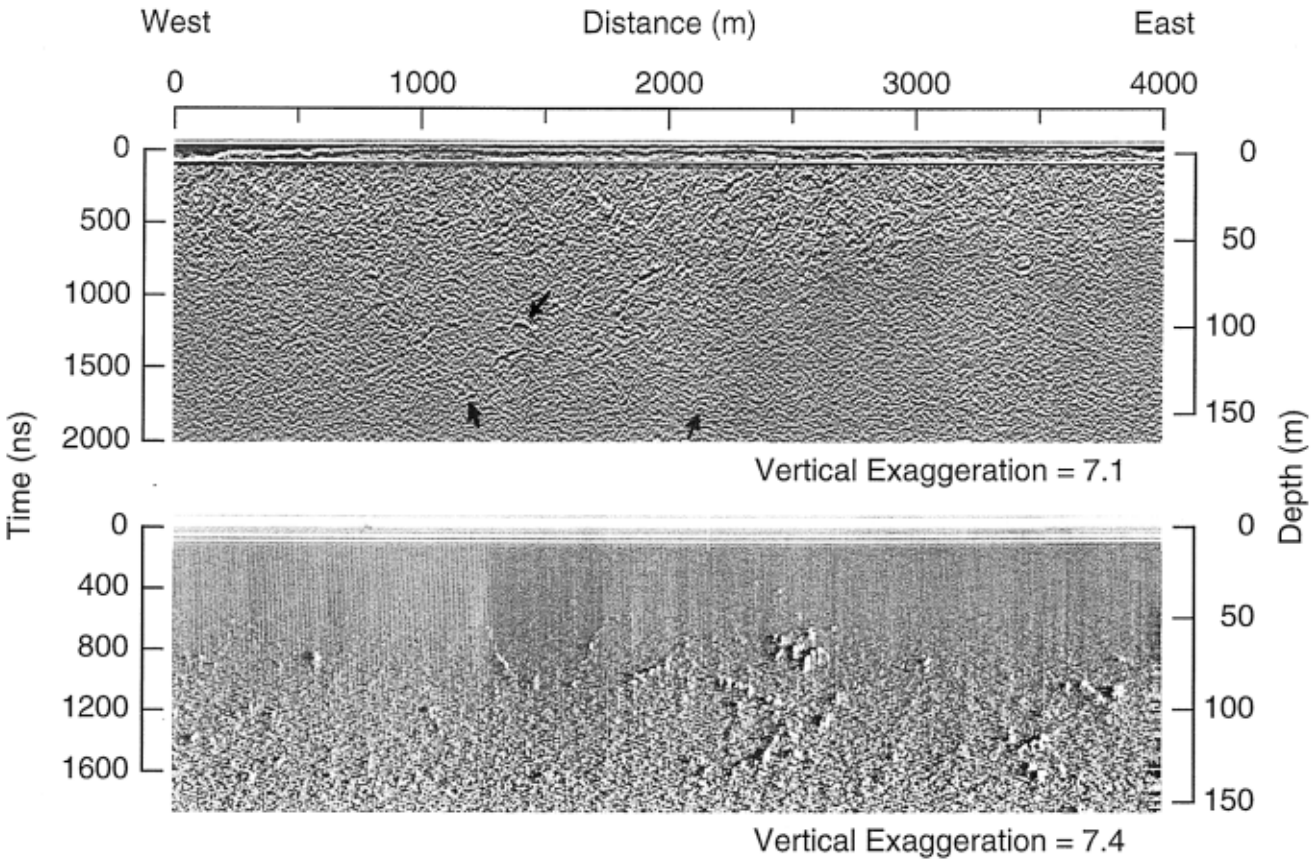

Fig. 13. 1.21–1.29 GHz FM-CW (top) and 100 MHz short-pulse (bottom) radar profiles of S4. The shadow effect in the lower profile is an artifact of a horizontal smoothing filter. The arrows in the FM-CW profile identify one event at about 100 m depth and two events at about 150 m depth that are just above clutter level.

CW radar. The surface slope here is nearly the same as for the other sections, but we have not provided elevation corrections because they are comparable to the depth range and give too much distortion to the profile. Although the recorded FM-CW frequency sweep corresponded with an ice depth of 539 m, only the depth to which targets appear is shown. The lower trace-acquisition rate (Table 1), the greater helicopter speed down-glacier, and the effective pulse length of 24 ns provided more noise than seen in the other FM-CW profiles.

We do not expect the FM-CW and 100 MHz profiles to be similar, as the transects were not coincident. The 100 MHz profile clearly indicates many responses at 100–150 m depth throughout the section. The FM-CW profile, however, shows only a few weak events within this depth range. The event at 100 m depth in the FM-CW profile is only about 2 dB above the clutter level. As seen in the previous profiles, the FM-CW profile indicates some horizons (near the 2 km distance) that appear to dip steeply because of the vertical exaggeration.

STRUCTURAL INTERPRETATIONS

We focus our interpretative discussion on horizon b in the profile of S3 (Fig. 10) because it contains numerous strong diffractions. The dipping horizons in both S2 and S3 suggest similar structures. The proximity of S2 and S3 to the pothole field (Fig. 7, bottom) also suggests that they are drainage conduits, like the one found by Sturm and Cosgrove (1990) to exist between two potholes.

Target size

We use the well-known radar equation (Skolnick, 1990) and the measured values of β_{rg} to calculate target radar cross-sections. We then relate the cross-sections to estimates of target area. The ratio of power (in watts), P_{rs}, received from large, planar reflectors (the snow or ice surface) at range H(m), to power transmitted, P_t, from an antenna in air is

$$P_{rs}/P_t = (G^2\lambda_0{}^2\rho_{asi}{}^2)/(64\pi^2H^2)\,, \qquad (6)$$

where G is the antenna gain function (antenna directivity divided by total radiated power) and λ_0 is the center frequency wavelength (m) in air. The quantity $\rho_{asi}{}^2 = \rho_{as}{}^2 + (\tau_{as}\tau_{sa}\rho_{si})^2$ accounts for the total power reflected from the air/snow and snow/ice interfaces for normal incidence. System losses are not considered, because they cancel out in the formulation of β_{rg}. For an englacial target of radar cross-section σ (m^2), where the dimensions of σ are much less than the target range $H + D$, the ratio of power received, P_{rt}, to P_t is

$$P_{rt}/P_t = (\Phi G^2\lambda_0{}^2\sigma)\tau_{asi}{}^2e^{-4\gamma D}/[64\pi^3(H+D)^4]\,, \qquad (7)$$

where D is depth to the target and $\tau_{asi}{}^2 = (\tau_{as}\tau_{sa}\tau_{si}\tau_{is})^2$ accounts for the total power transmitted through the air/snow and snow/ice interfaces, for normal incidence. The snow layer ($n_s = 1.3$) increases $\tau_{asi}{}^2$ from 0.85 (air/ice) to 0.92. The quantity γ is the propagation attenuation rate in ice, and Φ is the energy focus factor defined earlier (see FM-CW antenna gain). Correcting both Equations (6) and (7) individually for the inverse square dependency of intensity upon range (i.e. Equation (6) is multiplied by H^2, and Equation (7) by $(H+D)^2$, as was done to the traces of Figure 11), the power ratio $\beta_{rg} = (P_{rt}/P_t)/(P_{rs}/P_t)$ is then

$$\beta_{rg} = (\Phi\sigma\tau_{asi}{}^2e^{-4\gamma D})/[\pi\rho_{asi}{}^2(H+D)^2]\,. \qquad (8)$$

An approximate expression for the σ of a highly conduc-

https://doi.org/10.3189/172756500781833133 Published online by Cambridge University Press

tive flat plate of area A whose dimensions are large compared with a wavelength in ice, λ_i, (about 0.12 m at 1.4 GHz) is

$$\sigma = 4\pi A^2 {n_i}^2/{\lambda_0}^2 \quad (9)$$

(e.g. Skolnick, 1980), where $n_i = 1.78$ is the refractive index of ice. We modify this expression to account for the target area being the upper surface of a void so that

$$\sigma = 4\pi {\rho_{ia}}^2 A^2 {n_i}^2/{\lambda_0}^2, \quad (10)$$

where $\rho_{ia} = -\rho_{ai}$ is the ice/air target interface amplitude reflectivity. We assume that the target dimensions are large compared with λ_i, and that the target upper surface area is of large radius of curvature in order to allow ρ_{ia} to be the plane-wave Fresnel value. We then substitute Equation (10) into Equation (8) to obtain

$$A = \left[\lambda_0 (H + D) \mathrm{e}^{2\gamma D} \sqrt{\beta_{rg} {\rho_{asi}}^2/{\rho_{ia}}^2}\right] \Big/ (2 n_i \tau_{asi} \sqrt{\Phi}) \,. \quad (11)$$

The squares of the reflection coefficients are retained under the radical to avoid inclusion of their signs. Substituting $\lambda_0 =$ 0.2 m for the mid-frequency of the FM-CW system, $H = 6$ m, $\tau_{asi} = 0.96$, ${\rho_{asi}}^2/{\rho_{ia}}^2 = 0.51$, and the appropriate values of D (46 m, 41 m) and Φ (2.7, 2.6) for the minimum and maximum values of β_{rg} (0.17, 0.50) for the englacial events within traces 754 and 701, respectively, in Figure 11 give

$$A = (0.57, 0.91) \mathrm{e}^{2\gamma D} \,. \quad (12)$$

We extrapolate the loss tangent ($\tan\delta$) data of Jiracek (1967), also reported by Bogorodsky and others (1985, p. 122), at several frequencies for ice at −1°C to give an approximate value of $\gamma = 0.008$ at 1.4 GHz ($\tan\delta \approx 0.0003$), where $\gamma = \pi n_i \tan\delta/\lambda_0$ for $\tan\delta \ll 1$. This value makes A range between 1.19 and 1.79 m^2. These areas are equivalent to squares of side length $9\lambda_i$ (1.09 m) and $11\lambda_i$ (1.34 m), respectively, at midband frequency, and are therefore consistent with the assumption that the dimensions of the target were large compared with an in situ wavelength (0.12 m at midband). Although a 23 dB weaker cross-section is predicted at 100 MHz by Equation (10) and is qualitatively consistent with our results, these target dimensions are comparable to the in situ 100 MHz wavelength (1.68 m), so such a simple formula cannot be applied at this frequency.

Despite the narrow antenna beamwidth, the FM-CW radar −3 and −10 dB one-way footprint illumination widths of about 14 and 25 m, respectively, at the target depths are still significantly larger than the target size, and account for the clutter shown in Figure 11. Obviously, the distribution of scatterers that caused this clutter was not dense enough (Skolnick, 1980) to prevent penetration.

The target sizes calculated above are greater than those of near-horizontal, moulin drainage channels (0.2–0.4 m wide) observed within sutured crevasses on a different glacier by Holmlund (1988); we find no evidence in the photography that our horizons were aligned along sutured crevasses. The implied volume of water that Sturm and Cosgrove (1990) observed to be draining into, and transported between, nearby potholes certainly justifies the meter-size target dimensions we have calculated. Assuming these horizons were active conduits during the previous summer, a simple calculation of conduit closure rate, based on the theory of Nye (1953; reviewed by Paterson, 1994, p. 115), shows that the overburden pressure at about 50 m depth acting for 200 days will give only about 10% loss in conduit radius.

Horizons

We think that the radar horizons reproduce the actual subsurface conditions because both radars produced similar responses over S1 and S3, yet they have vastly different beamwidths. For the FM-CW antennas, the round-trip (G^2 factor in Equation (7)) effective beamwidth in the ice, including the focus factor, provided a 3 dB footprint of only 9–16 m width at 30–60 m depth, respectively. For the 100 MHz antennas, the round-trip effective beamwidth of about 38° gives a far wider footprint (50 m) at 60 m depth. Therefore, at their deepest appearance in the records, the targets probably did not deviate more than about 8 m (1/2 diameter of a footprint) laterally from beneath the antennas. An FM-CW antennas misalignment of 15 m would place the target response at −30 dB below peak response and into the clutter level. Therefore, the FM-CW results show that the horizons were well aligned with the flight direction and the glacier axis, and the 100 MHz results imply that they were the only horizons connected with this structure.

We interpret the diffraction horizons to be responses from different points along individual features, and we believe that the stronger horizons must originate within or near the round-trip 3 dB beamwidth of the antennas because of their high amplitudes. For example, the 18 diffractions within the 180 m length of horizon b, section S3, could represent responses to either the periodic cross-sectional undulations of a straight (in direction) channel (Fig. 14, left) or to the apices of a meandering channel (Fig. 14, right). For the undulating-wall model, the periodicity in cross-sectional size would be about 10 m, and the maximum target area of 1.8 m^2 calculated above would fall well within the 3 dB beamwidth. Surface channels with undulating walls that cut through rock and glacial ice at similar scales are common and are remnants of breached, offset potholes (Wohl and others, 1999). This model also favors polarization sensitivity because the channel is favorably oriented with respect to the polarization of the FM-CW antennas, but not to that of the 100 MHz antennas.

The meander interpretation for horizon b in Figure 14 is closely related to the undulating-wall interpretation. Meandering channels also occur on glacial surfaces (Parker, 1975). The channel cross-section would be greater at the apices because of greater water speeds on the outside of the curves during past drainage. In the case shown in Figure 14, the meander periodicity is 20 m. The meander peak-to-peak amplitude is meant to be within the 3 dB effective beamwidth, about 15 m, at the maximum profiled depth of 60 m. This model could also favor polarization sensitivity because the axes of the larger cross-sections are favorably aligned with respect to the FM-CW antenna polarization. However, polarization sensitivity is not certain in any case, because of the large difference in wavelengths between 100 MHz and 1.4 GHz, and therefore in radar cross-section.

Given the above interpretation, the diffraction horizons in S1 (Fig. 8) are also meandering or undulating channels, and with stronger evidence than for S3 that they may be fed by near-surface channels, which could have been open during the previous summer. The longer horizons b and c in S1 are similar to horizons a in section S2 and b in S3, and the branching horizons c1–c4 make S1 appear to be a more developed version of the horizons in S2 and S3, i.e. over time additional drainage channels have developed from existing ones. The good agreement between the FM-CW and

https://doi.org/10.3189/172756500781833133 Published online by Cambridge University Press

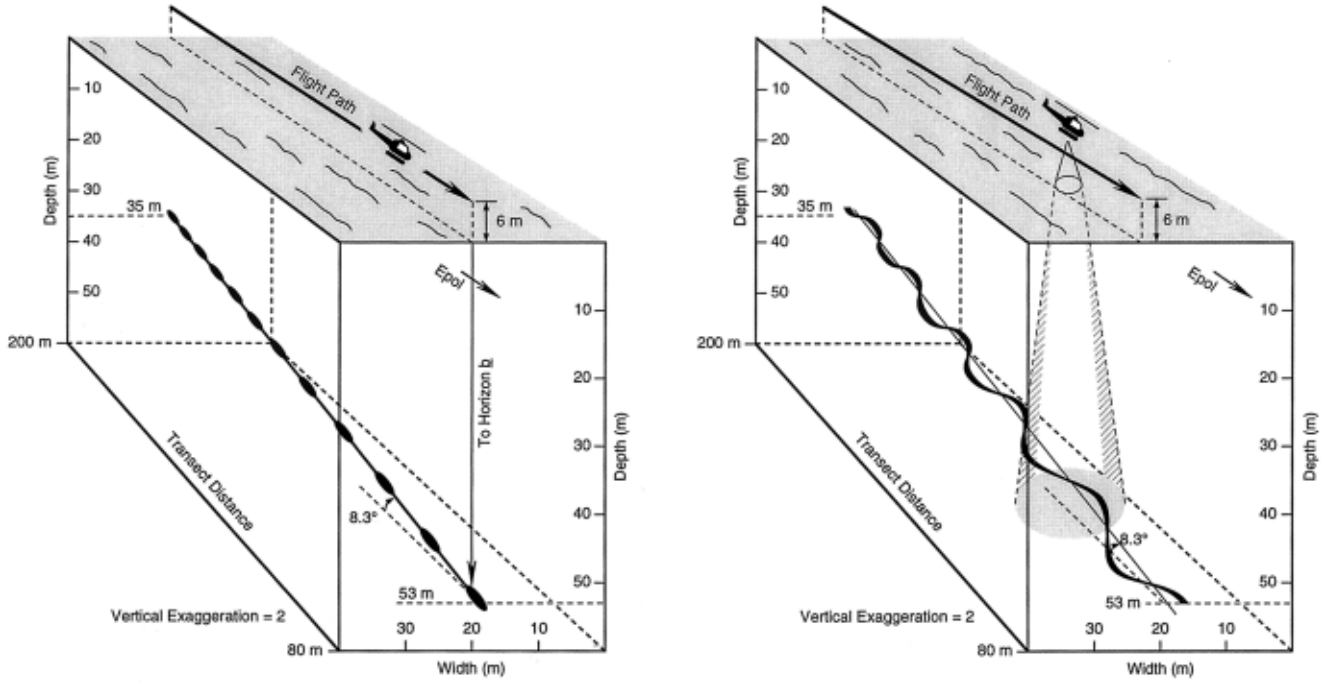

Fig. 14. Hypothetical models of drainage conduits that could produce a 120 m long segment of horizon b in the FM-CW profile of S3 in Figure 10. The interpretations represent structures that could produce 12 diffractions between the 380 and 500 m distances. The dip of 8.3° is relative to the surface.

100 MHz profiles in Figure 8 suggests that the targets within those horizons may be larger than those in profile S3 and not sensitive to electric-field polarization direction.

The presence of meanders in drainage channels has been discussed by Holmlund (1988) and Fountain and Walder (1998), the former of whom observed them to be parts of crevasses. Since we see no evidence of crevasses, or alignment with the nearby crevasses observed by Sturm and Cosgrove (1990) farther west, the horizons in S2 and S3 may be remnant evidence of the inter-pothole connections observed by Sturm and Cosgrove (1990) just up-glacier from S3, and kept open by continued summer drainage. If so, these horizons are convincing evidence that either down- or up-glacier drainage channels can develop at slight dip angles. Although a few of the branches do appear to steepen with depth, their generally shallow dip does not conform to the theory of Shreve (1972) which predicts a conduit orientation perpendicular to hydrologic equipotential surfaces at approximately 11 times the surface slope. This disagreement was also noted by Holmlund (1988).

CONCLUSIONS

The comparisons between the 1.4 GHz and 100 MHz radar profiles demonstrate significant reduction of clutter by the high-gain antennas, despite the large differences between wavelengths and between scattering cross-sections. The FM-CW disadvantage of being limited to a low average power can be compensated by using higher-gain antennas, while range is easily improved by decreasing the bandwidth, which would compromise vertical resolution only marginally if the decrease is not severe. However, the FM-CW lack of wavelet coherency with changing range cannot be compensated. The signal-to-clutter ratios show that the targets seen at 100 m depth along S4 could have been profiled with the 3 ns pulse bandwidth. In this case a range of 134 m would require only 2048 samples/trace with our present system. Therefore, given favorable surface conditions and winter operation, 1–2 GHz radars may help to resolve questions related to englacial drainage structure.

We conclude that the apparently branching nature of the horizons within sections S1 and S3, the meanders or undulations suggested by the aligned diffractions in S1, S2 and S3, the phase of the 100 MHz signals and the proximity of S2 and S3 to the pothole field are evidence that the horizons profiled are parts of drainage networks. The narrow FM-CW beamwidth suggests that the structures are generally aligned along the profile transect direction, which was that of glacier flow. In addition, the structures appear isolated because no other horizons were recorded along transverse profiles, nor did any of the 100 MHz horizons appear as significant distortions of the FM-CW horizons. The appearance of these structures along three sections of only one 9 km line suggests that others might be found in this area.

ACKNOWLEDGEMENT

This work was supported by the U.S. Department of Defense, DA Project 4A161102AT24. The authors thank one anonymous reviewer whose suggestions and comments greatly helped to improve this paper.

REFERENCES

Arcone, S. A. 1995. Numerical studies of the radiation patterns of resistively loaded dipoles. *J. Appl. Geophys.*, **33**, 39–52.

Arcone, S. A. 1996. High resolution of glacial ice stratigraphy: a ground-penetrating radar study of Pegasus Runway, McMurdo Station, Antarctica. *Geophysics*, **61** (6), 1653–1663.

Arcone, S. A. and A. J. Delaney. 1987. Airborne river-ice thickness profiling with helicopter-borne UHF short-pulse radar. *J. Glaciol.*, **33** (115), 330–340.

Arcone, S. A. and N. E. Yankielun. 1997. Reflection profiling of Arctic lake ice using microwave FM-CW radar. *IEEE Trans. Geosci. Remote Sensing*, **GE-35** (2), 436–443.

Arcone, S. A., A. J. Delaney and R. H. Wills. 1992. Helicopter-borne alpine glacier surveys using short pulse radar. *Geol. Surv. Can. Pap.* 90-4, 25–32.

Arcone, S. A., D. E. Lawson and A. J. Delaney. 1995. Short-pulse radar wave-

https://doi.org/10.3189/172756500781833133 Published online by Cambridge University Press

let recovery and resolution of dielectric contrasts within englacial and basal ice of Matanuska Glacier, Alaska, U.S.A. *J. Glaciol.*, **41**(137), 68–86.
Bamber, J. L. 1988. Enhanced radar scattering from water inclusions in ice. *J. Glaciol.*, **34**(118), 293–296.
Beckmann, P. and A. Spizzichino. 1963. *The scattering of electromagnetic waves from rough surfaces.* New York, Pergamon.
Blindow, N. and F. Thyssen. 1986. Ice thickness and inner structure of the Vernagtferner (Ötztal Alps): results of electromagnetic reflection measurements. *Z. Gletscherkd. Glazialgeol.*, **22**(1), 43–60.
Bogorodsky, V. V., C. R. Bentley and P. E. Gudmandsen. 1985. *Radioglaciology.* Dordrecht, etc., D. Reidel Publishing Co.
Calvo-Perez, O., A. Sentenac and J.-J. Greffet. 1999. Light scattering by a two-dimensional, rough penetrable medium: a mean field theory. *Radio Sci.*, **34**(2), 311–335.
Clarke, T. S. and C. R. Bentley. 1994. High-resolution radar on Ice Stream B2, Antarctica: measurements of electromagnetic wave speed in firn and strain history from buried crevasses. *Ann. Glaciol.*, **20**, 153–159.
Cumming, W. A. 1952. The dielectric properties of ice and snow at 3.2 centimeters. *J. Appl. Phys.*, **23**(7), 768–773.
Davis, J. L. 1973. The problem of depth sounding temperate glaciers. (M.Sc. thesis, Cambridge University.)
Delaney, A. J. and S. A. Arcone. 1995. Detection of crevasses near McMurdo Station, Antarctica, with airborne short-pulse radar. *CRREL Spec. Rep.* 95-7.
Ellerbruch, D. A. and H. S. Boyne. 1980. Snow stratigraphy and water equivalence measured with an active microwave system. *J. Glaciol.*, **26**(94), 225–233.
Forster, R. R., C. H. Davis, T. W. Rand and R. K. Moore. 1991. Snow-stratification investigation based on an Antarctic ice stream with an X-band radar system. *J. Glaciol.*, **37**(127), 323–325.
Fountain, A. G. and J. S. Walder. 1998. Water flow through temperate glaciers. *Rev. Geophys.*, **36**(3), 299–328.
Glover, J. M. and H. V. Rees. 1992. Radar investigations of firn structures and crevasses. *Geol. Surv. Can. Pap.* 90-4, 75–84.
Gogineni, S., T. Chuah, C. Allen, K. Jezek and R. K. Moore. 1998. An improved coherent radar depth sounder. *J. Glaciol.*, **44**(148), 659–669.
Gubler, H. and M. Hiller. 1984. The use of microwave FMCW radar in snow and avalanche research. *Cold Reg. Sci. Technol.*, **9**(2), 109–119.
Hance, J. H. 1937. The recent advance of Black Rapids Glacier, Alaska. *J. Geol.*, **45**(64), 775–783.
Harrison, W. D., L. R. Mayo and D. C. Trabant. 1975. Temperature measurements on Black Rapids Glacier, Alaska, 1973. *In* Weller, G. and S. A. Bowling, *eds. Climate of the Arctic.* Fairbanks, AK, University of Alaska. Geophysical Institute, 350–352.
Heinrichs, T. A., L. R. Mayo, K. A. Echelmeyer and W. D. Harrison. 1996. Quiescent-phase evolution of a surge-type glacier: Black Rapids Glacier, Alaska, U.S.A. *J. Glaciol.*, **42**(140), 110–122.
Holmlund, P. 1988. Internal geometry and evolution of moulins, Storglaciären, Sweden. *J. Glaciol.*, **34**(117), 242–248.
Jiracek, G. R. 1967. Radio sounding of Antarctic ice. *Univ. Wis. Geophys. Polar Res. Cent. Res. Rep.* 67-1.
Lawson, D. E. 1993. Glaciohydrologic and glaciohydraulic effects on runoff and sediment yield in glacierized basins. *CRREL Monogr.* 93-02.
Long, S. R. *and 6 others.* 1995. The Hilbert techniques: an alternate approach for non-steady time series analysis. *IEEE Geosci. Remote Sensing Soc. Newsl.* 94, 6–11.
Narod, B. B., G. K. C. Clarke and B. T. Prager. 1988. Airborne UHF radar sounding of glaciers and ice shelves, northern Ellesmere Island, Arctic Canada. *Can. J. Earth Sci.*, **25**(1), 95–105.
Nye, J. F. 1953. The flow law of ice from measurements in glacier tunnels, laboratory experiments and the Jungfraufirn borehole experiment. *Proc. R. Soc. London, Ser. A*, **219**(1139), 477–489.
Ødegård, R. S., J. O. Hagen and S.-E. Hamran. 1997. Comparison of radio-echo sounding (30–1000 MHz) and high-resolution borehole-temperature measurements at Finsterwalderbreen, southern Spitsbergen, Svalbard. *Ann. Glaciol.*, **24**, 262–267.
Oppenheim, A. V. and R. W. Schafer. 1975. *Digital signal processing.* Englewood Cliffs, NJ, Prentice-Hall.
Parker, G. 1975. Meandering of supraglacial melt streams. *Water Resour. Res.*, **11**(4), 551–552.
Paterson, W. S. B. 1994. *The physics of glaciers. Third edition.* Oxford, etc., Elsevier.
Raymond, C. F., R. J. Benedict, W. D. Harrison, K. A. Echelmeyer and M. Sturm. 1995. Hydrological discharges and motion of Fels and Black Rapids Glaciers, Alaska, U.S.A.: implications for the structure of their drainage systems. *J. Glaciol.*, **41**(138), 290–304.
Sheriff, R. E. 1980. *Encyclopaedic dictionary of exploration geophysics. Fourth edition.* Tulsa, OK, Society of Exploration Geophysicists.
Shreve, R. L. 1972. Movement of water in glaciers. *J. Glaciol.*, **11**(62), 205–214.
Skolnick, M. L. 1980. *Introduction to radar systems. Second edition.* New York, McGraw-Hill.
Skolnick, M. L. 1990. *Radar handbook.* New York, McGraw-Hill.
Smith, B. M. E. and S. Evans. 1972. Radio echo sounding: absorption and scattering by water inclusions and ice lenses. *J. Glaciol.*, **11**(61), 133–146.
Stove, A. G. 1992. Linear FMCW radar techniques. *IEE Proc.*, **139**(5), 343–350.
Sturm, M. 1987. Observations on the distribution and characteristics of potholes on surging glaciers. *J. Geophys. Res.*, **92**(B9), 9015–9022.
Sturm, M. and D. M. Cosgrove. 1990. Correspondence. An unusual jökulhlaup involving potholes on Black Rapids Glacier, Alaska Range, Alaska, U.S.A. *J. Glaciol.*, **36**(122), 125–126.
Wait, J. R. 1970. *Electromagnetic waves in stratified media. Second edition.* Oxford, Pergamon Press.
Watts, R. D. and A. W. England. 1976. Radio-echo sounding of temperate glaciers: ice properties and sounder design criteria. *J. Glaciol.*, **17**(75), 39–48.
Wohl, E. E., D. M. Thompson and A. J. Miller. 1999. Canyons with undulating walls. *Geol. Soc. Am. Bull.*, **111**(7), 949–959.
Yankielun, N. E., S. A. Arcone and R. K. Crane. 1992. Thickness profiling of freshwater ice using a millimeter-wave FM-CW radar. *IEEE Trans. Geosci. Remote Sensing*, **GE-30**(5), 1094–1100.

MS received 5 October 1998 and accepted in revised form 28 April 2000